American Journal of Energy Research, 2024, Vol. 12, No. 2, 40-46
Available online at http://pubs.sciepub.com/ajer/12/2/2
Published by Science and Education Publishing
DOI:10.12691/ajer-12-2-2

Enhancing the Performance of Titanium Dioxide Compact Layer on Epitaxial Graphene and Fluorine Tin Oxide Heterojunctions

Nelson Mugambi*, James Mbiyu Ngaruiya, Simon Waweru Mugo

Department of Physics, Jomo Kenyatta University of Agriculture and Technology Nairobi, Kenya
*Corresponding author: nelmug2013@gmail.com

Received May 10, 2024; Revised June 13, 2024; Accepted June 20, 2024

Abstract We report a facile synthesis of Titanium dioxide (TiO_2) modified compact layers on Fluorine Tin oxide (FTO) and graphene employing the Sol gel Doctor Blade technique, optimized systematically for enhanced solar energy conversion applications. UV-VIS spectrophotometer, a Varian 7000e FTIR, a Scanning Kelvin Probe Microscope, and Hall Effect setup evaluated the as deposited and films subjected to 1 step, 2°C/min and 1°C/min annealing rates. FTIR revealed considerable absorption at low frequencies (less than 798 cm^{-1}) in TiO_2 on graphene heterojunctions, confirming the occurrence of Ti-O and C-O-Ti bonds. The predominant anatase TiO_2 characteristic was found at 438 cm^{-1}. The TiO_2 on graphene film annealed at 1 °C/min exhibited the lowest porosity (46%), as well as the highest dispersion energy (11.30 eV). As the annealing rates declined, so did the surface-to-volume energy loss ratio for all the annealed films. Graphene TiO_2 annealed at 1 ^oC/min had a lower VELF/SELF than TiO_2 on FTO, implying that an electron loses less energy when passing through the TiO_2 on graphene layer than it does in TiO_2 on FTO. The light absorption coefficient α and electron diffusion coefficient D of TiO_2 on graphene improved to 4.637×10^3 and 1.485×10^{-4} (1 ^oC/min), respectively, whereas TiO_2 on FTO values increased to 4.221×10^3 and 1.251×10^{-4} (1°C/min), in that order, with decreasing annealing rates. Higher values of TiO_2 on graphene α and D indicate enhanced electron transition in the films. Hall Effect measurements on as-deposited and annealed TiO_2 on graphene films demonstrated higher conductivity as annealing rates decreased, which was attributed to film recrystallization induced by calcination. Smoluchowski smoothing model, reveal surface scan average work functions (φ) and linear profile scan average work functions (φ) ensemble variations in granular tilts and surface slopes explaining geographic variation and distribution. Local fluctuations in φ triggered by the spatially varying concentrations of electric dipole moments are intrinsic to atomic steps and influence φ. TiO_2 incorporation on graphene photoanode increased h^+/e^-separation, electron transport, and light absorption. The continuous conduction network on compact TiO_2 nanoparticles acts as an electron leakage barrier, and the porous structure has a large specific surface area.

Keywords: *Graphene, TiO_2, Fluorine tin oxide, Porosity, electron transport*

Cite This Article: Nelson Mugambi, James Mbiyu Ngaruiya, and Simon Waweru Mugo, “Enhancing the Performance of Titanium Dioxide Compact Layer on Epitaxial Graphene and Fluorine Tin Oxide Heterojunctions.” *American Journal of Energy Research*, vol. 12, no. 2 (2024): 40-46. doi: 10.12691/ajer-12-2-2.

1. Introduction

Titanium dioxide (TiO_2) nanocomposites containing metal oxides such as fluorine tin oxide (FTO) or carbon nanostructures, particularly graphene, are currently a prominent focus of research in visible light-driven photo catalysts. In 2005, the Scotch tape method of graphene exfoliation led to exponential growth in a number of transdisciplinary activities [1]. The high carrier mobility (200,000 $cm^2 V^{-1}s^{-1}$), wide theoretical surface area (>2600 m^2/g), excellent thermal conductivity (3000 - 5000 $W m^{-1} K^{-1}$), and outstanding optical transparency make it an appealing alternative for use as a hybrid counterpart [2,3]. When employed as photo anodes in DSSCs, tree-like TiO_2 nanostructures created directly on FTO using pulsed laser deposition showed a high light-to-electricity conversion efficiency [4]. TiO_2 can be layered with carbon-based materials to serve as a support matrix for TiO_2 and to slow the recombination of excited electron-hole pairs [5,6,7].

Fourier transform infrared spectroscopy (FTIR) reveals conventional graphene characteristics as overlaid strong peaks at 950-1100 cm^1. These peaks reflect C-O stretching on the graphene surface caused by the presence of a small quantity of oxygen in TiO_2 [8]. The distinct signals at 1250, 1327, and 1385 cm^1 indicate displaced C-O-C, C-O...H, or C-O bonding, suggesting that unsaturated -C and -OH groups in alcohols are related [8,9]. The distinct signals at 1250, 1327, and 1385 cm^1 indicate displaced C-O-C, C-O...H, or C-O bonding, suggesting that unsaturated -C and -OH groups in alcohols are related [10].

Hall Effect measurements, which frequently perform on structured samples like cloverleaves or small squares in van der Pauw configuration, is utilized to extract sheet carrier density and mobility [11,12]. Measurements of the Hall Effect are essential for the electrical characterization of semiconductor materials and films because it reveals information about the kind of charge carriers, charge carrier density, and Hall mobility based on the Hall voltage. Although a low sheet resistance value is ideal, larger layers are required, which lowers light transmittance and efficiency [13]. The mesoporous TiO_2 thin film contains nanocrystalline spherical particles of 15-20 nm in diameter. Due to the oxygen vacancies in the lattice, the material is an n-doped semiconductor with a carrier concentration of ND = 10^{16} [14]. A distinctive electron recombination behavior is generated by the hole transport in a solid electrolyte in a solid-state DSSC, which is a hopping-like movement in the lattice sites [15,16]. A distinctive electron recombination behavior is generated by the hole transport in a solid electrolyte in a solid-state DSSC, which is a hopping-like movement in the lattice sites [17].

The current study utilized TiO_2 thin films deposited on FTO and graphene substrates, and the composite evaluated holistically. The goal is to investigate the influence of different annealing rates on bonding energy, porosity, light absorption, electron transport, and conductivity of TiO_2 on FTO and graphene, along with their impact on the efficiency of dye-sensitized solar cells.

2. Experimental Procedure

Graphene monolayer was deposited on a glass substrate using roll-to-roll (R2R) chemical vapour deposition (CVD) and wet transfer synthesis. FTO SnO_2:F glass substrates were obtained from Xinyan Technology Co. Limited, China. Then, using cotton brushes and analytical acetone grade 99.5% purity, both graphene and FTO on glass substrates were carefully cleaned for about 5 minutes. They films were then immersed in ethanol for five minutes before being washed with deionized water. The samples were dried by blowing pressurized warm air over them before being stored in a desiccator.

A 1 × 1 cm^2 window was left after applying scotch magic tape to the substrates to adjust the thickness of the TiO_2. Using the sol-gel Doctor-blade method, T/SP, 18% wt, and 15-20 nm TiO_2 nanocrystalline were coated on the substrates [18]. The drying procedure began with a 20-minute ambient temperature increase to improve film homogeneity, followed by a temperature ramp of 5 ^oC per minute up to 175 ^oC in a furnace [19]. The photoanodes were sintered for 30 minutes at 450 ^oC/min before cooling in the furnace.

To improve the surface roughness and crystallinity of the films, freshly prepared samples were annealed using a Nabertherm muffle furnace at 2°C/min and 1°C/min annealing rates from 25°C to 450°C [20]. A few films were kept in as prepared condition, while others were treated to one-step annealing at 450 ^oC, 30 minutes of sintering, and cooling to ambient temperature.

A UV-VIS spectrophotometer (Perkin Elmer Lambda 950) was used to measure the films' transmittance and absorbance between 400 and 800 nm. SCOUT software was used to collect optical parameters, such as refractive index (n) and absorption coefficient (α), as well as determine porosity and bandgap.

Fourier Transform Infra-Red (FTIR) spectroscopy was employed to measure infrared frequencies through the films that enabled plotting of transmittance versus wavenumber spectra. Applying the Van der Pauw technique to measure charge sheet density ns and charge mobility μ by the advent of Hall Effect in conjunction with a four-point probe. Origin Pro software version 8.5 was used to process the acquired data.

3. Results and Discussion

3.1. Optical Properties Study

3.1.1. Ftir Analysis

The interaction between TiO_2 nanoparticles with graphene was studied using vibration spectra. Figure 1 shows the FTIR spectra of TiO_2 graphene sheets as deposited and annealed at 1 step, 2 ^oC/min, and 1 ^oC/min rates in the 400-4000 cm^{-1} range. Low IR transmittance at high wavenumbers results in high absorption. A certain frequency without any peaks indicates the absence of a specific bond, and thus the absence of photon absorption.

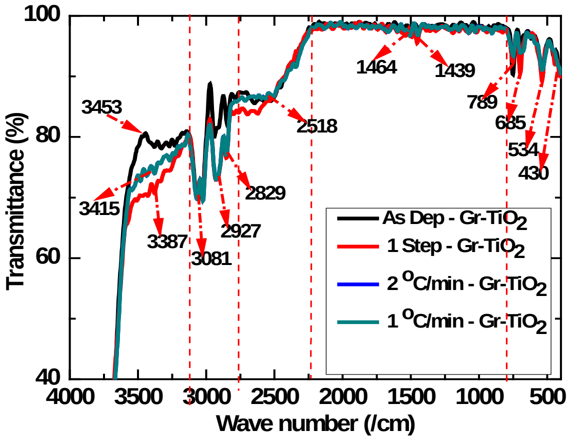

Figure 1. A graph FTIR spectrum for as deposited and annealed graphene TiO_2 versus Wavenumber

Real Deal - Hardinger's Five Zone analysis was used to analyze the IR spectra [21]. Zone 1 extends from 3700 to 3200 cm^{-1}, Zone 2 from 3200 to 2800 cm^{-1}, Zone 3 from 2800 to 2100 cm^{-1}, Zone 4 from 2100 to 800 cm^{-1}, and Zone 5 absorption peaks from 800 to 400 cm^{-1}. The stretching vibration modes of hydroxyl groups relate to the broadband between 2800 and 3200 cm^{-1}. [22]. OH groups have the potential to serve as electron donors for produced H^+, accept photo-induced holes, and generate OH radicals, all of which are very beneficial for enhancing photocatalytic activity. The stretching mode of aliphatic C-H groups is considered responsible for the absorption peaks at 2927, 2829, 3016, and 3081 cm^{-1} [23]. Additionally, a slight adsorption of TiO_2 molecules on the graphene surface via the O atom of the C = O [24] is suggested by a minor red shift at the C = O stretching vibration from 1464 to 1439 cm^{-1} (about 5 cm^{-1}). The vibration bonds at 471, 693, and 789 cm^{-1} correspond to the bonds Ti-O-Ti, Ti-O-O, and Ti-O, respectively [25], while the LO mode of amorphous TiO_2 is at 874 cm^{-1} [26]. For the samples annealed at annealing rates other than 1 °C / min, the 534 cm^{-1} peak is very weak, indicating the film annealing at 1 °C / min is well-crystallized. The findings also revealed the presence of a dominating feature centered at 438 cm^{-1} during annealing, which is a feature of the anatase TiO_2 [27]. The vibration of Ti-O-Ti and C-O-Ti was attributed to the extensive absorption at low frequency (below 798 cm^{-1}), which supported the development of the TiO_2 and C-O-Ti bond in graphene TiO_2 heterojunction [28]. Reduced annealing rates result in stronger C-O stretching, C-O-Ti bonds, and C=O carbonyl stretching, all of which could increase graphene TiO_2 electrical conductivity and boost the efficiency of photo-induced charge transfer.

3.1.2. Optical Band Gap

The graphene TiO_2 on graphene and TiO_2 on FTO sheets optical band gap was determined by utilizing the $(\alpha h\upsilon)^2$ versus hυ curve displayed in figure 2. Equation 1 yielded the tauc bandgap [29];

$$\alpha h\upsilon = B\left(h\upsilon - E_g\right)^r \qquad (1)$$

where E_g represents the optical band-gap, while the index r indicates the type of optical transition that occurs during photon absorption. The indices for the direct and indirect inter-band transitions are r = 1/2 and 2, respectively [30] and h denotes Planck's constant. α signifies the absorption coefficient. B is a proportionality constant (band tailing parameter) with values ranging from 10^7 to 10^8 m^{-1} [31].

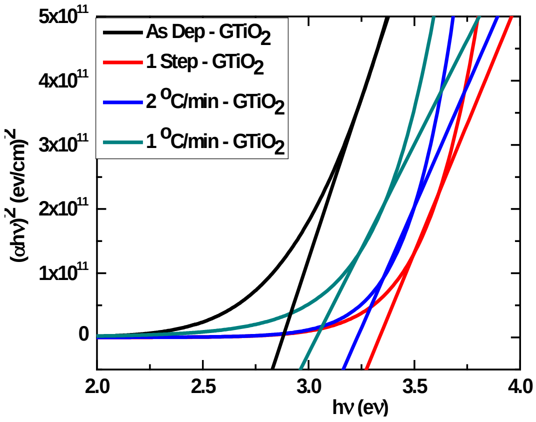

Figure 2. A graph $(\alpha h\nu)^2$ spectrum versus hν for determining Tauc Bandgap of TiO_2 on graphene.

We calculated the bandgap (E_g) by fitting a linear function to spectra in the UV region and reading the abscissa intersection. Bandgap values decreased as annealing rates decreased. Graphene has no influence on TiO_2 bandgap, being a semimetal with a zero bandgap. The values for as deposited TiO_2 on graphene as was 2.89 ev, and annealed films were 1 step 3.33 ev, 2 °C/min 3.22 ev, and 1 °C/min 3.04 ev, which were quite close to the bandgap of anatase TiO_2 which is approximately 3.2 ev. The tauc bandgap of TiO_2 on FTO was found to be 3.49 eV for as deposited and in the range of (3.35 - 3.54 eV) for annealed films. The wide tin band gap isassociated to increased bandgap. of TiO_2 on FTO. It is apparent that lowering annealing rates causes a red shift in the fundamental absorption edge of TiO_2 on graphene nanocomposites. TiO_2 on graphene has lower optical band gaps than TiO_2 on FTO. Therefore, the integration of graphene into TiO_2 is expected to boost the DSSC performance by increasing the absorption intensity of light.

3.1.3. Average Excitation oscillator Energy and Dispersion Energy

The average oscillator energy, E_o and dispersion energy were calculated by plotting a graph of $(n^2-1)^{-1}$ verses $(hv)^2$, as shown in figure 3 for 1°C/min films. The spectrum diminishes as $(h\nu)^2$ increases. The high specific BET area of graphene allows for a high dispersion of films within the visible region. Fitting linear at $(h\nu)^2$ = 5.1 ev^2 with equation 2 we get E_o and E_d values.

$$(n^2-1)^{-1} = \frac{E_0}{E_d} - \frac{1}{E_0 E_d}(h\upsilon)^2 \qquad (2)$$

where E_0 denotes the energy of a single oscillator and E_d denotes the energy of dispersion. h Planck's constant, υ frequency, and hυ photon energy.

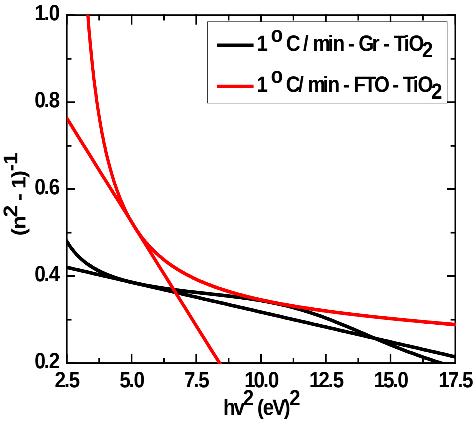

Figure 3. Plot of $(n^2-1)^{-1}$ versus $h\nu^2$ of annealed FTO TiO_2 and graphene TiO_2 coatings

Table 1 shows that average excitation energy for TiO_2 on graphene films is higher than that of TiO_2 on FTO, indicating that graphene TiO_2 films are more likely to undergo electron interband transitions than FTO-TiO_2.

Table 1. Optical parameters of Graphene TiO_2 and FTO TiO_2

Samples	Eg Tauc (FTO-TiO_2	Eg Tauc (Gr -TiO_2	E_d ($GrTiO_2$)	E_0 ($GrTiO_2$)	Eo (FTO TiO_2)	Eg (WWD)	FTO TiO_2 – P%	$GrTiO_2$ – P%
As-Prep	4.49	2.89	45.6	15.8	6.41	4.89	48.71	44.18
1 Step	4.54	3.33	6.38	4.66	4.23	2.33	73.08	69.32
2°C/min	4.40	3.22	9.77	5.46	4.64	2.73	61.38	57.19
1°C/min	4.35	3.04	12.7	5.76	4.85	2.88	51.77	46.12

3.1.4. Porosity

Figure 4 depicts porosity against photon energy graph TiO_2 on FTO and TiO_2 on graphene annealed at 1 °C/min rate. The porosity (P %) (the number of pores per volume) of TiO_2 films depends on the refractive index of the films. The equation (3) presented below [32,33] determines porosity of the films as a percentage.

$$Porosity = \left(1 - \frac{n_p{}^2 - 1}{n_0^2 - 1}\right) \times 100\% \qquad (3)$$

where n_p denotes the refractivity of anatase porous sheets and n_o = 2.52 denotes the refractivity of bulk TiO_2. Porosity was seen to decrease as hv increased. Porosity values were obtained at photon energies within the visible region corresponding to 2.26ev.

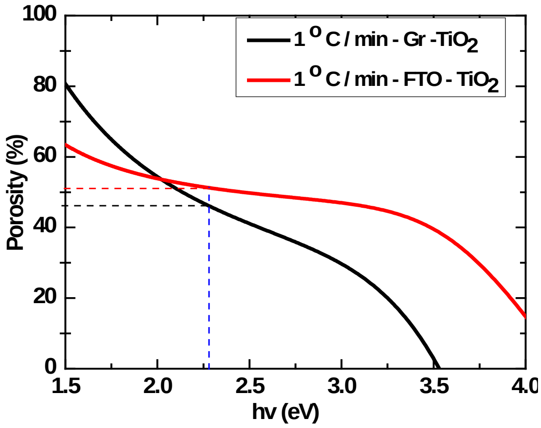

Figure 4. Plots of Porosity vs hv Gr/TiO_2 and FTO/TiO_2 annealed at 1 °C/min

Porosity was found to decrease as hv increased. Porosity values were obtained at 2.26 ev photon energies in the visible region . As shown in figure 4, porosity for TiO_2 on graphene at the specified energy is lower than that of TiO_2 on FTO, indicating that the latter gradually improved the quality of the film crystallization over the former. This is also connected with film contraction as a result of local matter migration caused by particle diffusion sintering. Light stimulated electrons (e) from the TiO_2 valence band (VB) to the conduction band (CB), leaving positively charged holes (h^+) in the VB. In the absence of an acceptor (graphene), e^- and h^+ would recombine instantaneously.

Figure 5 shows a plot of the band gap against porosity for as deposited and annealed films. It is seen that annealing TiO_2 produces oxygen vacancies and Ti^{3+} states, hence reducing the bandgap. Furthermore, incorporating TiO_2 into graphene results in the formation of a C-Ti bond, which improves e- transfer from TiO_2 to graphene by preventing recombination, extending the duration of separated carriers, lowering the bandgap, and achieving photocatalytic response in the visible region.

Figure 5 shows that porosity decreases with decreasing annealing rates, indicating that the film crystallization quality gradually improved. This is also connected with film shrinkage as a result of local matter migration caused by particle diffusion sintering. The Tauc bandgap values observed at the absorption edge are consistent with the Wemple Didominico (WDD) bandgap values obtained in the transparent zone. WDD bandgap were obtained relation (4) [34,35]

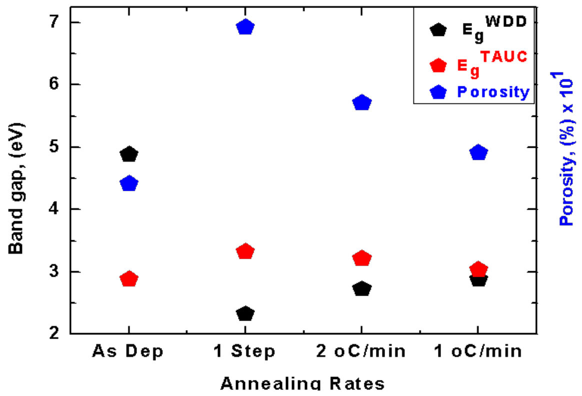

Figure 5. A model of Porosity and band gap Correlation for TiO_2 on graphene films.

$$E_g{}^{W-D} \approx \frac{E_o}{2} \qquad (4)$$

The minimal variance was obtained by evaluating in two different spectral regions. Since graphene Dirac point resonates with the TiO_2 conduction band, TiO_2 on graphene band gap falls within the TiO_2 range. The distortion of graphene Dirac cones near the K Point of the Brillouin zone caused by a rapid increase in temperature (thermal fluctuation) at a 1-step annealing rate promotes band gap opening at this rate.

The porosity (P) of nanoporous TiO_2 influences the light absorption coefficient (α) and electron diffusion coefficient (D) [36,37]. Porosity, P, with a maximum coordination number CN = 6, was established to be 0.41 (41%) for densely packed particles [38,39,40]. The light absorption coefficient (α) was calculated using equation 5 [41].

$$\propto = 2568(1-P)(P+2.89) \qquad (5)$$

Electron transport that is dependent on the connectivity of the particles can be affected by the electrode porosity. Effect of P on the electron diffusion coefficient, D can be expressed using equation 6 [42].

$$D = a\left|P - P_c\right|^{\mu} \qquad (6)$$

Where a, μ and the critical porosity, P_c are 4 x 10^{-4} cm^2s^{-1}, 0.82 and 0.76 in that order. α and D for as deposited and annealed TiO_2 on FTO and TiO_2 on graphene were recorded in Table 2. Both α and D for TiO_2 on FTO and TiO_2 on graphene were found to increase with decreasing annealing rates.

Table 2. α and D for TiO_2 on FTO and TiO_2 on Graphene films

	FTO – TiO_2		Gr – TiO_2	
Samples	α x 10^3	D x 10^{-4}	α x 10^3	D x 10^{-4}
As-Prep	4.448	1.379	4.776	1.564
1 Step	2.503	0.2206	2.823	0.4349
2°C/min	3.475	0.8266	3.806	1.016
1°C/min	4.221	1.251	4.637	1.485

3.1.5. Dielectric Energy Losses

The energy transferred to and from a compound semiconductor's topmost atom layer is expressed by the surface energy loss function (SELF) and volume energy loss (VELF), which are products of electron excitation in both the bulk and surface. Both SELF and VELF losses were analyzed using relation (5) and (6) respectively [43].

$$S_{elf} = \left\{-\frac{1}{\varepsilon}\right\} = \frac{\epsilon_2}{(1+\epsilon_1)^2+\epsilon_2^2} \tag{5}$$

$$V_{el} = \left\{-\frac{1}{1+\varepsilon}\right\} = \frac{\epsilon_2}{\epsilon_1^2+\epsilon_2^2} \tag{6}$$

Figure 6 shows that effective VELF/SELF decreased with increasing photon energy in the visible and ultraviolet regions of TiO_2 on graphene and TiO_2 on FTO films annealed at a rate of 1 °C/min. It was revealed that the effective VELF/SELF declined as photon energy increased. TiO_2 on graphene and TiO_2 on FTO were found to exhibit SELF/VELF values of 6.62 and 10.92, respectively, at hυ = 2.26 eV. An earlier study found that when an electron is excited by plasma oscillation, it loses more energy when traveling through the bulk of a medium rather than its surface [44].

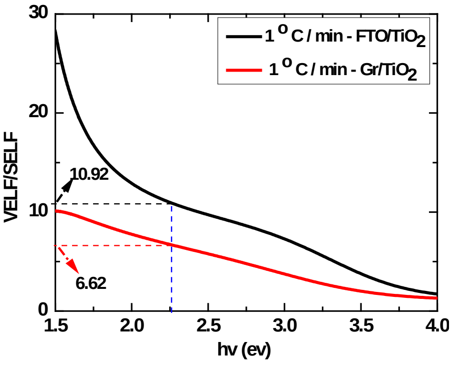

Figure 6. Plot of VELF/SELF versus hν. for TiO_2 on graphene and on FTO annealed at 1°C/min

The VELF/SELF of TiO_2 on graphene annealed at 1°C/min was found to be lower than that of TiO_2 on FTO annealed at the same rate, suggesting that the former crystallized more readily than the latter due to enhanced ad atom surface mobility on the glass substrate's surface and a beneficial TiO_2 anchor on graphene.

3.2. Charge Potential Distribution and Electrical Analysis

Surface potential difference or contact potential difference is used to quantify the surface charge distribution. It is associated with the sample work function (ϕ Sample) and provides information about the surface charging of thin films. Thin-film work function is given by equation 7 [45];

$$\phi_{sample} = \phi_{tip} - SP \tag{7}$$

The Hall effect occur when a voltage differential (the hall voltage) formed across TiO_2 on graphene in response to an applied magnetic field perpendicular to the current and an electric current in the conductor. The vertical resistance (RA) and horizontal resistance (RB) are calculated using equation (8);

$$R_A = \frac{V_{43}}{I_{12}} and R_B = \frac{V_{12}}{I_{23}} \tag{8}$$

Van Der Pauw technique was used to calculate sheet resistance R_s for the sample utilizing the equation (9) given below

$$\exp\exp\left(\frac{-\pi R_A}{R_S}\right) + \exp\exp\left(\frac{-\pi R_B}{Rs}\right) = 1 \tag{9}$$

Edwin Hall, [46] proposed equations (10), (11) and (12) for determining charge concentration ns, charge mobility μ and conductivity σ respectively.

$$n_s = \frac{IB}{q|V_H|} \tag{10}$$

Where B is the magnetic field, V_H is the hall voltage, I the current and q electron charge.

$$\mu_s = \frac{|V_H|}{R_S IB} = \frac{1}{q n_s R_S} \tag{11}$$

$$\sigma = \frac{1}{\rho} = q n_S \mu_S \tag{12}$$

3.2.1. Work function of TiO_2 on Graphene Films

Figure 7 illustrates the plotting of two-dimensional (2D) plots of area scan profiles across four samples created under varying annealing rates to examine the surface contact potential on the surface of nanocomposite thin films.

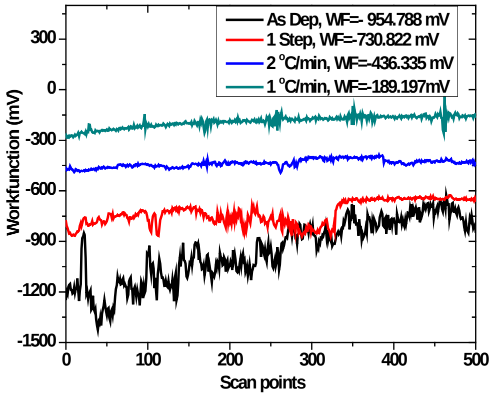

Figure 7. As deposited TiO_2 on graphene and annealed thin films with topographical area scan maps

The trend caused by annealing was validated by the spectra. The average work function values for as deposited, 1 step, 2 °C/min, and 1 °C/min were found to be -954.788 mV, -730.822 mV, -436.335 mV, and -189.197 mV, respectively. The measured effective work function is affected by changes in surface structure rather from being monotonic. This paper reports variation of the work function with respect to annealing rates. The enhanced crystallinity of TiO_2 is responsible for the work function's decrease with lower annealing rates.

3.2.1. Hall Effect measurements for TiO_2 on Graphene Films

Hall Effect measurement were recorded in Table 3.

Table 3. Hall Effect measurements

Samples	V_H (mV)	R_s (Ω/cm) x 10^3	ns (cm^{-2}) x 10^{15}	μs $(vs)^{-1}$x10^1	σ x10^{-3} $(\Omega cm)^{-1}$
As-Prep	1.943	10.44	4.366	1.370	9.582
1 Step	1.875	9.641	4.524	1.431	10.37
2°C/min	1.798	8.443	4.718	1.567	11.84
1°C/min	1.734	6.690	4.892	1.907	14.95

Hall carrier concentration and mobility were seen to rise as annealing rates decreased, associated with improved crystallinity and crystallite size growth. Conductivity was found to increase when annealing rates decreased. The microstructure of the film improved as the annealing rate was decreased. This reduces potential barriers and wells (higher grain size) at grain boundaries while also reducing TiO_2/graphene agglomeration, leading in improved charge percolation and thus high conductivity.

3.2. Correlation of Porosity and Conductivity of TiO_2 on Graphene Films

Figure 8 shows the correlation between porosity and conductivity inas deposited and annealed TiO_2/graphene sheets. Porosity decreased as annealing rates decreased, which was attributable to local matter migration caused by particle diffusion sintering. Similarly, conductivity rose as porosity decreased. This is because as the pore size decreases, the electronic interaction between TiO_2 particles increases.

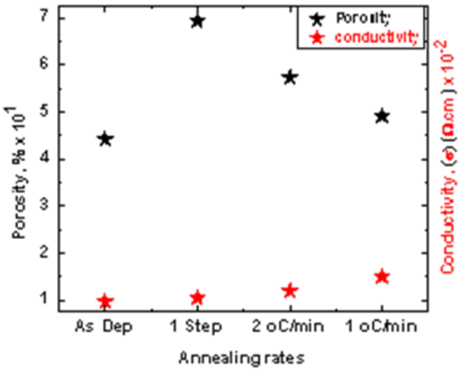

Figure 8. Correlation model of Porosity and conductivity of TiO_2 on graphene

The pore size of TiO_2 on graphene annealed at 1 °C/min was 0.4612, which was found to be close to the optimum porosity reported by Meng *et al.*, [45], at 0.41. This provide good anchor sites for dye molecules, resulting in increased photocurrent generation in DSSCs. The film's relatively high conductivity makes it excellent for solar cell applications. Our findings revealed that when TiO_2 was deposited on graphene, the light absorption coefficient and electron transport coefficient were higher than when TiO_2 embedded on FTO, owing to TiO_2's higher crystallinity on graphene relative to FTO. The higher light absorption coefficient is responsible for photon propagation in the scattering volume, the creation of excited electron-hole states, and the electron-hole lattice interaction associated with phonon formation. This improves the probabilities of electron diffusion coefficient, which can be attributed to higher film conductivity. High deposition temperatures (≥450°C) diminish bond dilatation in grain boundaries, reducing charge density fluctuations explaining enhanced conductivity even at lowest annealing rates [47]. Tiny gaps and voids exist at the FTO/TiO_2 interface as a result of high porosity and the irregular microstructure of FTO glass. These voids and gaps inhibit connection and hasten the recombination process. Graphene fills the gaps because of its exceptional mobility and flexibility. Charge transfer resistance at the interface reduces when TiO_2 is compacted on graphene, improving its passivation. Oxygen vacancies and Ti^{3+} defects are created when the sub-band gap in the annealed TiO_2 on graphene composite film starts to lie deeply in the tail of the density of states. These defects speed up the interband transition while narrowing the band gap.

4. Conclusion

The study show that porosity of TiO_2 on FTO and on graphene thin films decreases with a decrease in annealing rate due to films' densification and improved crystallinity. TiO_2 on graphene heterojunctions showed significant absorption at low frequencies (less than 798 cm^{-1}), as indicated by FTIR, indicating the presence of Ti-O and C-O-Ti bonds. The highest surface potential has been demonstrated for low annealing rates. The observed variations in work function are related to fluctuations in the surface dipole moment of the surface molecules and the Smoluchowski effect. Dipole moment lowers the potential barrier for charge carriers, which aids in suppressing electron-hole recombination, raising the chemical reaction's quantum yield, and boosting the catalytic reactivity of TiO_2 films. The experimental results show that films of TiO_2 on graphene and TiO_2 on FTO annealed at 1°C per minute are ideal for use in optoelectronics due to their optimum porosity, VELF/SELF-ratio, and high light absorption coefficient, electron diffusion coefficient, conductivity.

References

[1] Novoselov, K.S., Jiang, D., Schedin, F., Booth, T. J., Khotkevich, V.V., Morozov, S.V., & Geim, A.K. (2005). "Two-dimensional atomic crystals", *Proceedings of the National Academy of Sciences of the United States of America*, 102(**30**): 10451-10453.

[2] Dervin, S., Dionysiou, D.D., Pillai, S.C. (2016). "2D nanostructures for water purification: graphene and beyond", *Nanoscale*, 8:15115-15131.

[3] Ganguly, P., Harb, M., Cao, Z., Cavallo, L., Breen, A., Dervin, S., Dionysiou, D.D., Pillai, S.C. (2019a). "2D nanomaterials for photocatalytic hydrogen production", *ACS Energy Letters* 4 (**7**), 1687-1709.

[4] Sauvage, F., Fonzo, F. D., Bassi, A. L., Casari, C. S., Russo, V., Divitini, G., .Ducati, C. E., Comte, P. & Gra¨tzel, M. (2010). "Hierarchical TiO_2 Photoanode for Dye-Sensitized Solar Cells", *Nano Letters*, 10 (**7**) 2562–2567.

[5] Scanlon, D. O., Dunnill, C. W., Buckeridge, J., Shevlin, S. A., Logsdail, A. J., Woodley, S. M., Catlow, C. R., Powell, M. J., Palgrave, R. G., Parkin, I. P., Watson, G. W., Keal, T. W., Sherwood, P., Walsh, A., & Sokol, A. A. (2013). "Band alignment of rutile and anatase TiO_2", *Nature materials*, 12(**9**), 798–801.

[6] Cravanzola, S., Jain, S.M., Cesano, F., Damin, A., Scarano, D. (2015). "Development of a multifunctional TiO_2/MWCNT hybrid composite grafted on a stainless steel grating", *RSC Advances*, 5: 103255–103264."

[7] Zhu, J., Cao, Y., & He, J. (2014). Facile fabrication of transparent, broadband photoresponse, self-cleaning multifunctional graphene-TiO_2 hybrid films", *Journal of colloid and interface science*, 420,

119–126.

[8] Amiri, A., Shanbedi, M., Ahmadi, G., Eshghi, H., Kazi, S. N., Chew, B. T., Savari, M., & Zubir, M. N. (2016). “Mass production of highly porous graphene for high-performance supercapacitors”, *Scientific reports*, 6: 32686.

[9] Rahimi, R, Zargari, S., & Sadat Shojaei, Z. (2014). “Photoelectrochemical investigation of TiO_2-graphene nanocomposites”, .*In Proceedings of the 18th International Electronic Conference on Synthetic Organic Chemistry, Basel,* Switzerland, 1–30.

[10] Morrow, B. A., & Beauchamp, Y. B. A., (1971). “Infrared Spectra of Some Alkyl Platinum Compounds. Part II. Assignment of the CH Stretching Modes of a Methyl Group”, *Canadian Journal of Chemistry*, 49(**18**): 2921-2925.

[11] Werner F., (2017). “Hall measurements on low-mobility thin films”, *Journal of Applied Physics*, 122(**13**):135306.

[12] Schroder, D. K. (2006). “Semiconductor Material and Device Characterization”, *John Wiley & Sons*, 800.

[13] Han, L., Kiode, N., Chiba, Y., and Mitate, T. (2004). “Modeling of an equivalent circuit for dye sensitized solar cells”, *Applied Physics Letters*, 84 (**13**), 2433-2435

[14] Chen L., Hsu C., Chan P., Zhang X. & Huang C. (2014). “Improving the performance of dye-sensitized solar cells with TiO_2/graphene/ TiO_2 sandwich structure”, *Nanoscale Research Letters*, **9**: 380 -389.

[15] Smestad, G. P., Spiekermann, S., Kowalik, J., Grant, C. D., Schwartzberg, A. M. Zhang, J., Tolbert, L. M., Moons, E. (2003). “A technique to compare polythiophene solid-state dye sensitized TiO_2 solar cells to liquid junction devices”, *Solar Energy Materials & Solar Cells* 76: 85–105.

[16] Li, B., Wang, L., Kang, B., Wang, P. and Qiu, Y. (2006). “Review of Recent Progress in Solid-State Dye-Sensitized Solar Cells”, *Solar Energy Materials and Solar Cells*, 90: 549-573.

[17] Hasan, M. M., Haseeb, A. S. M. A., Saidur, R., Masjuki, H. H. and Hamdi. M. (2009). "Synthesis and Annealing of Nanostructured TiO_2 Films by Radio-Frequency Magnetron Sputtering", *Journal of Applied Sciences*, **9**: 2815-2821.

[18] Frederichi, D., Scaliante, M. H. N. O., and Bergamasco, R. (2021). “Structured photocatalytic systems: photocatalytic coatings on low-cost structures for treatment of water contaminated with micro pollutants—a short review,” *Environmental Science and Pollution Research*, **28**(19), 23610-23633.

[19] Ngei K. (2016). “Characterization And Performance Evaluation Of Graphene Films As Counter Electrodes For Dye Sensitized Solar Cells”. *Unpublished Thesis, Juja: JKUAT.*

[20] Benjamin M. J., Simon W. M., and James M. N. (2018) “Effect of Annealing Rates on Surface Roughness of TiO_2 Thin films.” *Journal of Materials Physics and Chemistry*, 6, (2): 43-46

[21] Hardinger, S. (2008), Organic Molecular Structures and Interactions. *University of California*, **47**: 223-226.

[22] Maira, A. J., Coronado, J. M., Augugliaro, V., Yeung, K. L., Conesa, J. C., Soria, J, & Catal,. J. (2001). “Fourier Transform Infrared Study of the Performance of Nanostructured TiO_2 Particles for the Photocatalytic Oxidation of Gaseous Toluene”, *Journal of Catalysis*, 202: 413-420.

[23] Kumar, B., Smita, K., Cumbal, L., Debut, A., Camacho, J., Hernández-Gallegos, E., Chávez-López, M. G., Grijalva, M., Angulo, Y., Rosero, G. Y. A. & Gustavo, R. (2015), “Pomosynthesis and biological activity of silver nanoparticles using Passiflora tripartitafruit extracts [J]”, *Advanced Materials Letters*, 6(**2**): 127−132.

[24] Behera, M. and Ram, S. (2012). “Synthesis and characterization of core-shell gold nanoparticles with poly (vinyl pyrrolidone) from a new precursor salt”, *Applied Nanoscience*, 3: 83–87.

[25] Gao, Y., Masuda, Y., Peng, Z., Yonezawa, T. & Koumoto, K. (2003). “Room Temperature Deposition of TiO_2 Thin Films from Aqueous Peroxotitanate Solution”, *Journal of Materials Chemistry*, 13: 608-613.

[26] Gonzalez R. J., Zallen R. and Berger, H. (1997). “Infrared reflectivity and lattice fundamentals in anatase TiO_2”, *Physical Review B*. 55: 7014 - 7017.

[27] Xu, Y. & Shen, M. (2008). ‘Fabrication of anatase-type TiO_2 films by reactive pulsed laser deposition for photocatalyst application’, *Journal of Materials Processing Technology*, 202 (**1–3**): 301–306.

[28] Pan, X., Zhao, Y., Liu, S., Korzeniewski, C. L., Wang, S., & Fan, Z. (2012). “Comparing graphene-TiO_2 nanowire and graphene-TiO_2 nanoparticle composite photocatalysts”, *ACS applied materials & interfaces*, 4(**8**), 3944–3950.

[29] Tauc, J., Grigorovici, R., & Vancu, A. (1966). “Optical properties and electronic structure of amorphous germanium”, Physica Status Solidi, 15, 627-637.

[30] Gould, M., & Lamont, C. (2010). “Examination of the optical band gap of various semiconducting materials”, Reed College, Portland, OR 97202.

[31] Illican, S., Caglar, Y., & Caglar, M. (2008). “Preparation and characterization of ZnO thin films deposited by sol-gel spin coating method. Journal of Optoelectronics and Advanced Materials. 10(**10**), 2578-2583.

[32] Ye, Q., Liu, P. Y., Tang, Z. F., & Zhai, L. (2007). “Hydrophilic Properties of Nano-TiO_2 Thin Films Deposited by RF Magnetron Sputtering,” *Vacuum*, 81(**8**), 627–631.

[33] Liu, J., Gan, D., Hu, C., Kiene, M., & Paul S. H. (2002). Porosity effect on the dielectric constant and thermomechanical properties of organosilicate films,” *Applied Physics Letters*, 81 (22), 4180.

[34] Wemple S. H. & DiDomenico M. (1969) “Oxygen□ Octahedra Ferroelectrics. II. Electro□ optical and Nonlinear□ Optical Device Applications,” Journal of Applied Physics, 40: 735.

[35] Wemple S. H. & DiDomenico M. (1971) “Behavior of the Electronic Dielectric Constant in Covalent and Ionic Materials,” *Physical Review B*, 3: 1338–51.

[36] Rothenberger, G., Fitzmaurice, D. & Gratzel, M. (1992). “Spectroscopy of conduction band electrons in transparent metal oxide semiconductor films: optical determination of the flatband potential of colloidal titanium dioxide films”, *Journal of Physical Chemistry*, 96 (**14**), 5983–5986.

[37] Ferber; J., & Luther, J. (2001). “Modeling of Photovoltage and Photocurrent in Dye-Sensitized Titanium Dioxide Solar Cells”, *Journal of Physics and chemistry B*. 105: (**21**), 4895–4903.

[38] Bouvard, D. & Lange, F. F. (1992). “Correlation between random dense parking and random dense packing for determining particle coordination number in binary systems,” *Physical review A*, 45 (**8**), 5690 – 5693.

[39] Kingerly; N. D. & Berg, M (1955), “Study of the Initial Stages of Sintering Solids by Viscous Flow, Evaporation□ Condensation, and Self□ Diffusion”, *Journal of applied Physics* 26, 1205-1212.

[40] Nolan, G. T. & Kavanagh, P. E. (1992). “Computer simulation of random packing of hard spheres”, *Powder technology*, 72 (**2**): 149-155R.

[41] Gomez; R. & Salvador, P. (2005)”. Photovoltage dependence on film thickness and type of illumination in nanoporous thin film electrodes according to a simple diffusion model”, *Solar Energy Materials and Solar Cells*. 88(**4**): 377-388.

[42] Lee, J. J., Coia, G. M. & Lewis, N. S. (2004). “Current Density versus Potential Characteristics of Dye-Sensitized Nanostructured Semiconductor Photoelectrodes. 2. Simulations”, *Journal of Physics and Chemistry B*, 108 (**17**), 5282–5293.

[43] Yang C., Fan H., Xi Y., Chen J. & Li Z. (2008). “Effects of depositing temperatures on structure and optical properties of TiO_2 film deposited by ion beam assisted electron beam evaporation”, *Applied Surface Science*, 254: 2685-2689.

[44] Zerweck, U., Loppacher, C., Otto, T., Grafström, S., & Eng, L. M. (2005). “Accuracy and resolution limits of Kelvin probe force microscopy”, *Physical Review B*, 71(**12**), 125424.

[45] .Meng, N., Michael, K. H. L., Dennis Y.C., & Leung, K. S. (2005). “An analytical study of the porosity effect on dye- sensitized solar cell performance,” *Solar Energy Materials and Solar Cells*, 90, 1331–1344.

[46] Hall, E. (1879). "On a New Action of the Magnet on Electrical Current," *American Journal of Mathematics*, 2: 287-292.

[47] Benkstein; K. D., Kopidakis, N., Van de Lagemaat, J. & Frank, A. J. (2003), “Influence of the Percolation Network Geometry on Electron Transport in Dye-Sensitized Titanium Dioxide Solar Cells”, *Journal of Physics and Chemistry B*, 107 (**31**), 7759–7767.